

Cite this: DOI: 00.0000/xxxxxxxxxx

Virtual Electrode plating XPS Investigation of the Solid Electrolyte Interphase formed between Li Metal Anode and LGPS and LAGP Solid Electrolytes[†]

Yi Liang^a, Matthew Burton^{a,b}, Ben Jagger^a, Hua Guo^{a,b}, Johannes Ihli^a and Mauro Pasta^{a,b}

Received Date

Accepted Date

DOI: 00.0000/xxxxxxxxxx

In situ X-ray photoelectron spectroscopy (XPS) techniques have proven to be powerful tools for the characterisation of the solid electrolyte interphase (SEI) formed between the anode and solid electrolyte (SE) in solid-state batteries. XPS offers access to time and operational condition-resolved information on the SEI's chemical composition in the absence of destructive sample preparation. Here we present a Virtual Electrode Plating XPS (VEP-XPS) investigation of the composition and stability of the SEI formed between lithium metal and two different solid electrolytes: $\text{Li}_{10}\text{GeP}_2\text{S}_{12}$ (LGPS) and $\text{Li}_{1.5}\text{Al}_{0.5}\text{Ge}_{1.5}(\text{PO}_4)_3$ (LAGP). LAGP shows slower SEI formation kinetics, as proven by the emergence of a metallic lithium signal, while LGPS exhibits rapid SEI growth that prevents metallic lithium from plating. We attribute these observations to the SEI composition, distribution and physical properties of secondary decomposition products and in particular to the mixed ion-electron conductive Li_3P which can be observed in LGPS and not in LAGP.

Introduction

Solid-state batteries (SSBs) employing a solid electrolyte (SE) and a lithium metal anode have been regarded as the 'holy grail' of energy storage due to expectations of enhanced safety and higher energy density compared to conventional lithium-ion batteries (LIBs)^{1–3}. The compatibility of the LMA with the SE is key to the realisation of stable, high energy density Li metal SSBs⁴. The solid electrolyte interphase (SEI) formed between the SE and LMA plays a crucial role in this regard. Formed as a result of interfacial reactions, this nano-composite consisting of crystalline and amorphous reaction products determines battery performance. The ideal SEI exhibits high ionic conductivity and low electronic conductivity to facilitate lithium ion transport while limiting the

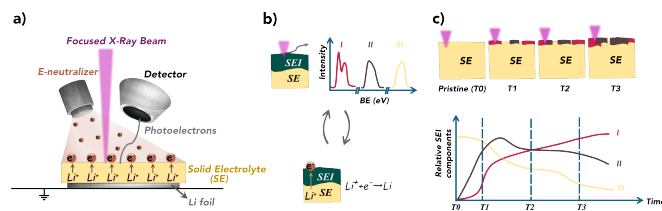


Fig. 1 Virtual Electrode Plating X-ray Photoelectron Spectroscopy (VEP-XPS). (a) Schematic of the VEP-XPS experiment illustrating the mechanism of operation, whereby the electron neutraliser provides an electron beam and generates a bias across the sample stack which facilitates Li-ion migration towards the top surface; (b) Experiment workflow: XPS measurements and E-beam plating are periodically alternated; (c) Illustration of SEI growth and composition as a function of plating time; chemical phases are determined from deconvoluted XPS spectra

extent of electrochemical reactions^{5–7}. Investigation of the SEI, in terms of composition, spatial extent, and reaction pathways, should therefore be a key part of the SSB battery development and optimisation^{8–10}. While the number of high ionic conductivity SEs investigated has steadily increased over the last two decades^{11–14}, the characterisation of SEIs has remained challenging on account of their thinness (often a few nanometres) and compositional heterogeneity^{6,15}.

The Virtual Electrode Plating X-ray Photoelectron Spectroscopy (VEP-XPS) is an emerging technique that allows time- and operational condition-resolved characterisation of the SEI formed in the first charge. This method replicates the Li plating process within the XPS chamber, allowing for detailed characterisation about the SEI formation dynamics. The *in situ* Li sputtering technique allows the characterisation of the composition of the formed SEI as soon as the LMA is brought into contact with SEs. These techniques could eliminate the need for destructive and potentially invasive sample preparation steps in many cases^{16–19}. Either via virtual electrode plating or Ar-ion sputtering (Figure 1a and Figure S7 respectively), a thin film of Li is gradually deposited onto

^a Department of Materials, University of Oxford, Parks Road, Oxford OX1 3PH, UK.
Email: mauro.pasta@materials.ox.ac.uk

^bThe Faraday Institution, Quad One, Becquerel Avenue, Harwell Campus, Didcot OX11 ORA, UK

[†] Supplementary Information available: [details of any supplementary information available should be included here]. See DOI: 00.0000/00000000.

the surface of a SE under ultra-high vacuum (UHV) conditions. Iterative XPS measurements during this process enable the formation and evolution of the SEI as the deposited Li reacts with the SE to be investigated^{20–23}.

Using VEP-XPS and *in situ* Li sputtering techniques, we report on the composition, chemical stability, and electrochemical stability of the SEIs formed between Li metal and two types of SE: $\text{Li}_{10}\text{GeP}_2\text{S}_{12}$ (LGPS) and NASICON-type $\text{Li}_{1.5}\text{Al}_{0.5}\text{Ge}_{1.5}(\text{PO}_4)_3$ (LAGP).

With an ionic conductivity of up to $12 \text{ mS}\cdot\text{cm}^{-1}$, LGPS has been proposed as an attractive SE, yet has failed to find practical implementation in light of previously reported unstable SEI growth during battery operation.

LAGP has also been heavily investigated as a SE due to its high air stability and promising ionic conductivity^{24–27}, but SEI growth has also been limiting its application²⁸.

The pristine structures of these SEs both contain Ge^{4+} , which is susceptible to reduction to Ge^0 and alloying to form Li_xGe when in contact with the LMA^{21,22,25,29}, which is an undesirable electronic conductive phase in the SEI, but how this affects the stability of the SEI depends on the evolution of the other SEI components, necessitating a study of the whole degradation process.

XPS experiments probing the stability of LAGP at the interface with Li metal revealed reduced reaction kinetics compared to the sulphide LGPS electrolyte. The SEI formed between LGPS and Li metal displays an apparent continuous growth behaviour due to the presence of the electronic conductive and ionic conductive $\text{Ge}(\text{Li})$ and Li_3P phases^{23,30}. These experiments highlight the importance of the chemical composition of the SEI, and their electronic and ionic properties. This work also introduces a potential approach for quantifying the SEI formation kinetics, which could improve our understanding of the SEI formation process.

Experimental

Materials

Solid electrolyte $\text{Li}_{1.5}\text{Al}_{0.5}\text{Ge}_{1.5}(\text{PO}_4)_3$ (99.99% pure, D50=500nm) was purchased from *AmpceraTM* through MSE Supplies LLC. Li ribbon (99.9% pure) was purchased from Sigma-Aldrich. The $\text{Li}_{10}\text{GeP}_2\text{S}_{12}$ SE was synthesised through a ball milling and heat treatment method. The precursors Li_2S (99.98%, Merck), GeS_2 (MP Biomedicals), and P_2S_5 (99%, Merck), in the stoichiometric ratio, along with an additional 2 wt% sulphur (sublimed, Alfa Aesar), were mechanically milled at 700 rpm for 5 hours in sealed ball-milling jars. The resulting mixture was pelletised and annealed at 550 °C for 8 hours in an argon-filled glovebox. After naturally cooling to room temperature, the pellet was ground, and the final product, $\text{Li}_{10}\text{GeP}_2\text{S}_{12}$ powder, was collected.

XPS sample preparation

LAGP pellets were prepared through the following procedure. Initially, 150 mg of LAGP powder was cold-pressed under 150 MPa using a 10 mm die press. The pressed pellets underwent a high-temperature sintering process in a box furnace at 900°C for 10 hours in an air environment. The furnace temperature ramping

rate was set at 2°C min^{-1} , and to compensate for Li loss, the pellet was placed on top of a LAGP powder bed. Subsequently, the sintered pellets were polished using sandpaper with grit ranging from 800 to 4000, resulting in a smooth surface on both sides. The size of the sintered pellets was about 850 μm in thickness and 8.38 mm in diameter. LGPS pellets were prepared by cold pressing 150 mg powder at 400 MPa using a 8 mm die.

For the virtual plating sample, the SE pellet was pressed on top of a pre-punched 8 mm Li disk, which was affixed to a thin copper disk at a much lower pressure of 40 MPa. Then the sample stack was stuck onto the XPS stage using carbon tape with the Li-foil-free surface facing up and transferred to the XPS intro chamber from the glovebox using an air-tight transfer vessel. The Li metal used in this experiment was firstly brushed using a toothbrush to eliminate surface contamination and subsequently calendered to achieve a smooth surface. The pressed pellet was stuck onto the sample stage without any further treatments for the in-situ sputtering experiment.

VEP-XPS experimental setup

XPS experiments were conducted using the PHI VersaProbe III with an Al K α X-ray ($\text{hv}=1486.8 \text{ eV}$) source. The pressure inside the XPS chamber was at 10^{-7} Pa level. During the VEP-XPS experiment, the XPS instrument integrated electron neutraliser gun, acting as a virtual electrode, was used to provide a constant flux of electrons to the SE pellets surface; driving Li^+ migration upwards through the SE. The combination of migrated Li^+ and neutraliser-provided electrons at the top surface of the SE results in the gradual formation of metallic Li species.

The measurement point was located at the centre of the pellet using X-ray-induced secondary electron images (SXI), and the electron beam was also focused on the pellet centre. The applied beam current was 20 μA for both LGPS and LAGP SEs. The electron beam plating and XPS acquisition were performed alternatively to study the SEI evolution. For the in-situ sputtering experiment, the ion gun beam voltage was set as 4 kV and the Li metal target was directly facing the Ar^+ ion gun during the sputtering process. The Li metal sputtering and XPS measurements were conducted alternatively to probe the evolution of the surface chemistry information.

The XPS probing area was $500 \mu\text{m} \times 500 \mu\text{m}$, and all measurements were performed with the neutraliser off. The pass energy for the survey scan was 224 eV and 55 eV for the high-resolution scan. Collected spectra were processed using CasaXPS software and were calibrated based on C 1s to 248.8 eV (unless specified)³¹.

Results and discussion

The electron neutraliser gun generated electron beam provided a bias across the sample stack that drove the upward migration of Li^+ through the SE to its surface. At the surface, the Li^+ and neutraliser-provided electrons combined, resulting in the gradual formation of metallic Li. This reacted with the underlying SE, causing the formation, growth, and evolution of an SEI. These SEI formation processes were probed by alternating between XPS

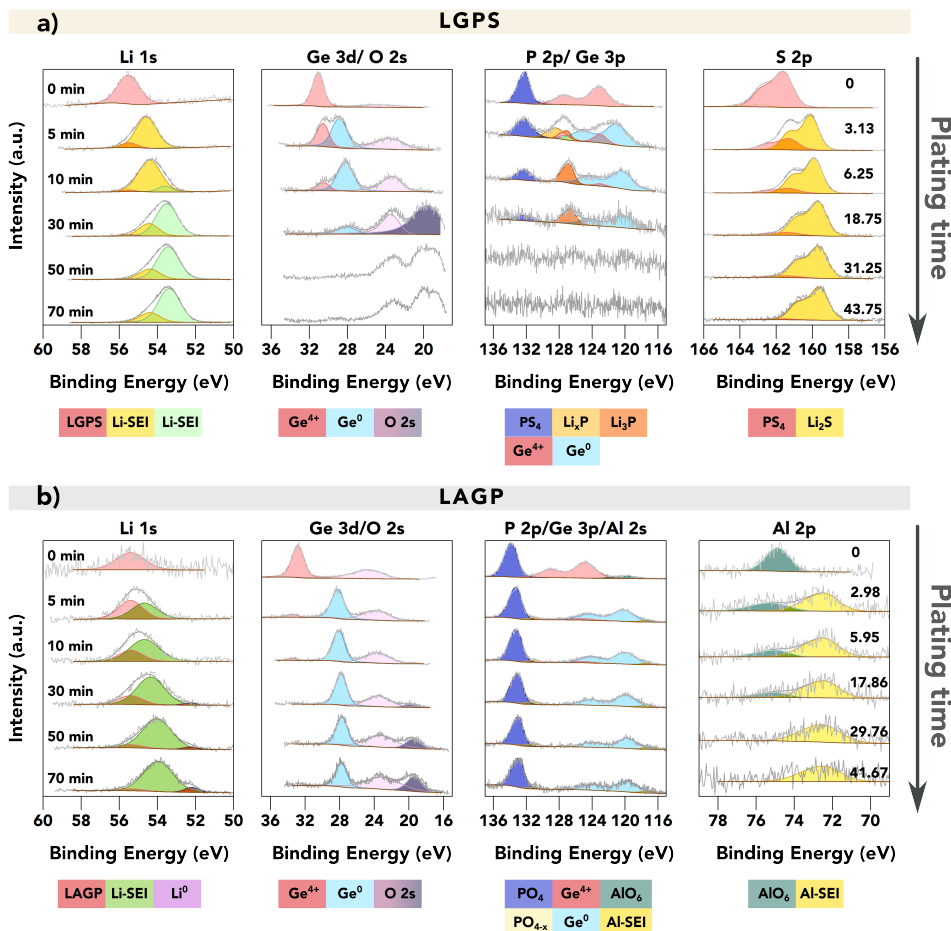


Fig. 2 VEP-XPS investigations of LGPS and LAGP. The plots show time series of XPS core spectra acquired during VEP-XPS experiments examining the SEI formation on top of (a) LGPS and (b) LAGP. The total Li plating time (E-beam exposure time) is given in the first column, and the passed charge q_A ($\mu\text{Ah}\cdot\text{cm}^{-2}$), normalised by area, is labelled in the last column. Acquired spectra (grey) are shown along with linear combination fitting results. The individual spectral components are coloured; a key is provided below each group of spectra. For LGPS SE, two Li 1s SEI peaks are labelled in two colours as a summary of all Li environments in different SEI components, as their close BE values make it difficult to deconvolute the peaks accurately. The peak intensities were normalized for each acquired core spectrum to improve the visibility of minor spectral contributions; the raw peak intensity variations are provided in the SI. The applied beam current was 20 μA for both samples.

spectra acquisition and E-beam (Li) plating. In view of the relatively recent development of VEP-XPS^{22,23}, we performed an *in situ* Li sputtering XPS experiment to cross-validate observations. This is summarised in Figure S8 and Figure S9.

Firstly, to confirm that the observed electrolyte decomposition is not caused by the applied electron beam, “VEP-like” experiments were performed on both LGPS and LAGP SEs without a Li metal source (the Li foil) on the underside of the SE (Figure S3). During these experiments, no change in the SE composition was detected, confirming that the observed changes in chemical information on the surface are due to the electrochemical reaction between the electrolyte and the plated Li metal.

Figure 2 provides a comparison of the XPS spectra collected for a) LGPS and b) LAGP during the VEP experiment. The evolution of the core spectra for the main elements (from left to right Li, Ge, P and Al/S, respectively) is shown as a function of Li “plating” time. For the pristine (labelled as 0 min) LGPS and LAGP, we observe a

single Li environment in the Li 1s spectra centred at 55.4 eV and 55.5 eV, respectively. A similar observation is made for the Ge 3d region, with a single peak at approximately 30.5 eV and 32.5 eV, consistent with values reported by He *et al.* and Yu *et al.* for the Ge^{4+} environment^{29,32}. The difference in Ge binding energy (BE) between LGPS and LAGP is due to the fact that the Ge atom is bonded to six more electronegative oxygen (O) atoms in LAGP, forming a GeO_6 octahedron, whereas GeS_4 is present in LGPS³³. Correspondingly, the phosphorus atom is found in the PS_4^{3-} or PO_4^{3-} structure, as visible in the P 2p spectra. The Al 2p and S 2p spectra show the bonding environments of AlO_6 octahedra (in LAGP) and PS_4^{3-} (in LGPS), respectively.

After 5 minutes of *in-situ* Li plating, the onset of SEI formation is detectable, with decomposition products visible in both LGPS and LAGP spectra. The Li 1s region shows the formation of a second, signal-dominating Li environment of reduced oxidation state, which is assigned as “Li-SEI” for both LGPS and LAGP.

The Ge 3d spectral regions also change, revealing the formation of a secondary Ge environment of reduced oxidation state (the electronically-conductive Ge metal phase) in both LGPS and LAGP at about 28 eV.

The differences between the SEIs on LGPS and LAGP are visible in the S 2p (LGPS), Al 2p (LAGP), and also P 2p spectral regions. Correlated with the reduction in Ge in the LGPS structure, the P-S structure in the LGPS SEI underwent significant degradation, as we observed the substantial formation of Li_2S and the reduced phosphide species including Li_xP and Li_3P in line with previous reports about LGPS SEI formation^{21,22}. In the case of LAGP SE, the formation of a new Al-containing component at the interphase is indicated by the BE shift of the Al 2p peak from 74.5 eV to 72.3 eV. This decrease in BE signifies a change in the Al bonding environment, transitioning from the initial AlO_6 octahedra, where the Al atom is bonded to six O atoms, to a new structure. XPS measurement on a piece of aluminium foil was performed to verify if the new Al-SEI phase is in its metallic form. The result, illustrated in Figure S6, shows that the Al 2p peak for metallic Al has a BE of 71.6 eV, which is approximately 0.7 eV lower than the BE of the Al-SEI peak. This difference suggests that the Al atoms in the Al-SEI phase are bonded to fewer O atoms, potentially forming LiAlO_2 where the Al atom bonded with four O atoms in the AlO_4 tetrahedral structure, which possesses promising stability against Li metal^{34–36}. Further investigations are required to identify this Al-containing decomposition product. However, the peak intensity of Al 2p is rather low, as an indication of the low atomic concentration of the Al-SEI phase in the SEI.

The peak in the P 2p spectra of LAGP exhibits a relatively stable BE of around 133.2 eV up to this point and it remains detectable during continued plating, suggesting that the P atoms maintain their PO_4 tetrahedral structure^{32,37}. The implication of this is that Li_3PO_4 is a major component of the LAGP SEI, in contrast to the LGPS SEI in which Li_2S predominates. This also indicates that the strong bonding strength of P-O bonds helps the PO_4 tetrahedral structure to remain intact. With continuous Li plating, the phosphorus species would be reduced to Li_3P , but interestingly this is not seen in LAGP SE. SEI growth continues on both electrolyte materials as more Li is plated.

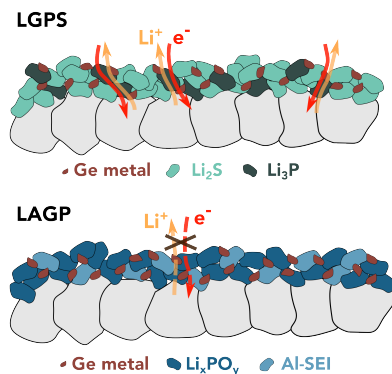


Fig. 3 Schematic of the multi-component SEI layer formed on top of LGPS and LAGP SEEs.

By the 30th minute of the *in-situ* Li plating, the spectral signa-

tures of pristine LGPS and LAGP are almost completely replaced by SEI-associated spectra, since the XPS-probed volume now consists mostly of SEI material. Here, the metallic Li (Li^0) peak was only observed for LAGP SE, as an indication of the formation of a more passivating SEI layer for LAGP SE.

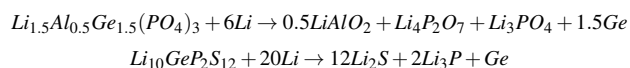
As Li plating continues up to 70 minutes, differences in the stabilities of the SEIs formed on LGPS and LAGP are revealed. These differences are most visible in the Li 1s and Ge 3d spectral regions, in two ways.

Firstly, while the SEI of LAGP contains a significant fraction of electronically conductive Ge^0 in the SEI throughout, the fraction of this phase in the LGPS SEI decreases with plating time, which agrees with a previous report²². The intensity attenuating of the Ge signal as well as the P signal may result from the formation of Li_2O on the surface, which obscures the signal from the underneath layer. The formation of Li_2O is likely due to the reaction between the formed Li_2S and the residual air inside the XPS chamber. This is evident in Figure S4, which shows that a pellet of pure Li_2S continuously forms Li_2O on its surface.

Secondly, for both LGPS and LAGP, we observe a gradual shift in the Li-SEI peak position towards a lower binding energy with increased plating time. The emergence of a Li^0 peak would signify that the reaction rate between Li and the underlying SEI layer is slower than the time needed to collect the Li 1s spectra (≈ 30 minutes). In contrast, the absence of a Li^0 peak would denote that the plated Li continues to react with the underlying SEI faster than the time required to collect the Li 1s spectra. The latter would result in faster SEI growth and thus a thicker SEI layer. In this work, the formation of metallic Li was only observed on LAGP SE, which is indicative of a more passivating SEI, compared to LGPS. For LGPS, no spectroscopic signature of metallic Li could be detected throughout the experiment as shown in Figure 2, which we attribute to the fast reaction kinetics between LGPS SE and lithium and the formation of a more ionically or electronically conductive SEI layer.

Janek *et. al.* suggested that the SEI growth relies on the availability of both electrons and ions and is therefore limited by the slowest of either ionic or electronic transport³⁸. One possible explanation for the different observed behavior of the two electrolytes could be found in percolation theory³⁹, which predicts that a percolation threshold greater than 15 vol% is required for a continuous pathway to exist.

Assuming the following decomposition reactions^{21,34}:



The SEI in LGPS should initially contain more than 20 vol% of ionically and electronically conductive phases (Ge^0 and Li_3P , see Table S1), suggesting the presence of a continuous electronic and ionic pathway. This would lead to the rapid and continuous growth of the SEI layer, preventing the Li^0 peak from manifesting.

In contrast, the only ionically and electronically conductive phase within the initial LAGP SEI nanostructure is Ge^0 , occupying less than 13 vol%. As a result, the LAGP SE shows restrained reaction kinetics against Li metal compared to LGPS. This concept is schematically depicted in 3b. Additional information about SEI

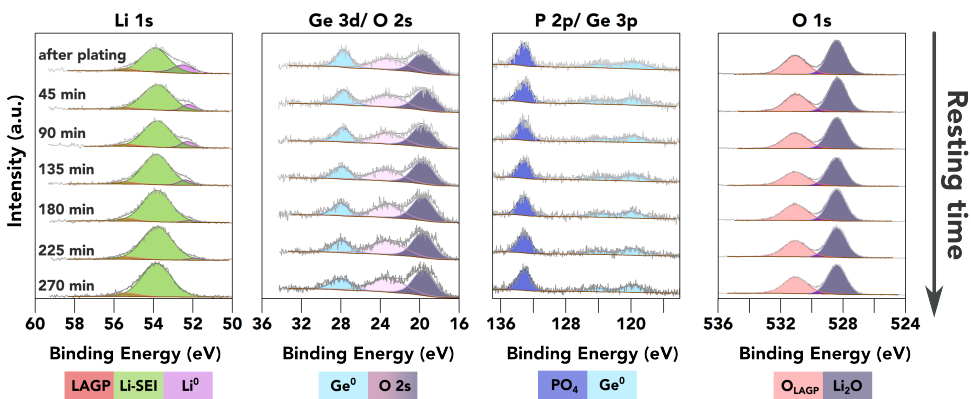


Fig. 4 XPS investigation of the further reaction of plated Li metal with the underneath layer. The plots show a time series of XPS core spectra acquired after a strong Li^0 peak was observed on top of LAGP. The resting time is given in the first column.

nanostructure and exact composition would be required to assess if the growth is limited by electrons or ions.

Previous studies reporting an unstable SEI were performed at the LAGP-Li interface during cycling within a confined cell setup where the build-up of strain and mechanical degradation could facilitate the SEI decomposition^{26,40}. In contrast, here, this experimental setup removes the effects of pressure, allowing solely the chemical properties of the SEI to be probed to help gain a better understanding of degradation mechanisms. It is therefore necessary to further investigate SEI stability in this system.

As an attempt to study the SEI evolution kinetics, continuous XPS measurements were conducted on the surface of the LAGP SE after a strong Li^0 peak was observed as shown in Figure 4, without any further Li plating. In principle, the SEI formation kinetics can be extracted from the Li^0 peak attenuation rate, and the increasing rate of other characteristic peaks from different SEI components. In the case of LAGP SE, Ge, P and O spectra are available for this quantification process. As shown in Figure 4, Ge stays in its metallic form (evidenced by both Ge 3d and Ge 3p spectra). The BE of the P 2p- PO_4 peak stays constant, suggests the stability of the PO_4 structure against Li metal. Both Ge and P signals show a slight decrease in peak intensity over time.

There are two possible pathways for the plated Li metal on the surface: it can be oxidised by the residual air inside the XPS chamber, or react with the underneath layer to form SEI. The oxidation rate of metallic Li inside the XPS chamber was investigated by continuous XPS measurements on a piece of sputter-cleaned Li foil as shown in Figure S4, which demonstrates that over 50 at% of the metallic Li was oxidised within the first 50 minutes, resulting in the formation of Li_2O and LiOH . However, the O 1s peak from LiOH , with a BE of approximately 530.7 eV, is less than 0.4 eV away from the O 1s- PO_4 peak. This proximity can introduce errors to the quantification process, thus reducing the accuracy of reaction kinetics estimations. The proximity of these two peaks characteristic of two possible pathways mean that no quantification of the reaction kinetics could reliably be conducted due to the errors introduced into the quantification process.

Further, no significant differences in overall SEI composition and stability could be detected between the results of the VEP-

XPS experiment reported above and those of the equivalent *in situ* Li sputtering XPS experiments (Figure S8 and Figure S9).

Conclusion

In summary, virtual electrode plating and *in situ* Li sputtering XPS experiments performed on LGPS and LAGP SEs provided consistent results in terms of SEI composition and growth. LAGP shows slower reaction kinetics, as proven by the emergence of a Li^0 peak, while LGPS exhibits rapid SEI growth that prevents metallic lithium from plating. The absence of applied pressure in a VEP-XPS experiment, allows us to attribute these observations to the SEI composition, distribution and physical properties of secondary decomposition products and in particular to the mixed ion-electron conductive Li_3P which can be observed in LGPS and not in LAGP. Additionally, the *in-situ* XPS technique provides the potential to investigate SEI formation kinetics by continuously monitoring the surface information after the Li^0 is observed. However, to accurately quantify the reaction kinetics, an ultra-high vacuum level (much lower than 10^{-7} Pa) is required to minimise the reaction between the Li metal and the chamber environment.

Conflicts of interest

There are no conflicts to declare.

Data availability

Data will be made available on request.

Acknowledgements

This work was supported by the Faraday Institution SOLBAT project (grant number FIRG056) and Henry Royce Institute (through UK Engineering and Physical Science Research Council grant EP/R010145/1). M.P. is grateful for the support of Nissan Motor Co. Ltd., Japan. B.J. is grateful for the support of the Clarendon Fund Scholarships.

Supplementary data

Supplementary data to this article can be found online at

Notes and references

- 1 X. B. Cheng, R. Zhang, C. Z. Zhao and Q. Zhang, *Toward Safe Lithium Metal Anode in Rechargeable Batteries: A Review*, 2017, <https://pubs.acs.org/sharingguidelines>.
- 2 D. Lin, Y. Liu and Y. Cui, *Nature Nanotechnology*, 2017, **12**, 194–206.
- 3 J. Lu, Z. Chen, F. Pan, Y. Cui and K. Amine, *Electrochemical Energy Reviews*, 2018, **1**, 35–53.
- 4 J. Janek and W. G. Zeier, *Nature Energy*, 2016, **1**, 16141.
- 5 A. Banerjee, X. Wang, C. Fang, E. A. Wu and Y. S. Meng, *Interfaces and Interphases in All-Solid-State Batteries with Inorganic Solid Electrolytes*, 2020, <https://dx.doi.org/10.1021/acs.chemrev.0c00101>.
- 6 S. A. Pervez, M. A. Cambaz, V. Thangadurai and M. Fichtner, *ACS Applied Materials & Interfaces*, 2019, **11**, 22029–22050.
- 7 S. Wenzel, T. Leichtweiss, D. Krüger, J. Sann and J. Janek, *Solid State Ionics*, 2015, **278**, 98–105.
- 8 W. D. Richards, L. J. Miara, Y. Wang, J. C. Kim and G. Ceder, *Chemistry of Materials*, 2016, **28**, 266–273.
- 9 Y.-Y. Sun, F. Li and P.-Y. Hou, *Journal of Materials Chemistry A*, 2021, **9**, 9481–9505.
- 10 H.-D. Lim, J.-H. Park, H.-J. Shin, J. Jeong, J. T. Kim, K.-W. Nam, H.-G. Jung and K. Y. Chung, *Energy Storage Materials*, 2020, **25**, 224–250.
- 11 J. Janek and W. G. Zeier, *Nature Energy*, 2023, **8**, 230–240.
- 12 M. Uitz, V. Epp, P. Bottke and M. Wilkening, *Journal of Electrocermics*, 2017, **38**, 142–156.
- 13 J. C. Bachman, S. Muy, A. Grimaud, H. H. Chang, N. Pour, S. F. Lux, O. Paschos, F. Maglia, S. Lupart, P. Lamp, L. Giordano and Y. Shao-Horn, *Inorganic Solid-State Electrolytes for Lithium Batteries: Mechanisms and Properties Governing Ion Conduction*, 2016, <https://pubs.acs.org/doi/abs/10.1021/acs.chemrev.5b00563>.
- 14 Y. Lee, J. Jeong, H. J. Lee, M. Kim, D. Han, H. Kim, J. M. Yuk, K.-W. Nam, K. Y. Chung, H.-G. Jung and S. Yu, *ACS Energy Letters*, 2021, 171–179.
- 15 M. B. Dixit, J. S. Park, P. Kenesei, J. Almer and K. B. Hatzell, *Status and prospect of: In situ and operando characterization of solid-state batteries*, 2021, <https://pubs.rsc.org/en/content/articlehtml/2021/ee/d1ee00638j> <https://pubs.rsc.org/en/content/articlelanding/2021/ee/d1ee00638j>.
- 16 F. Walther, R. Koerver, T. Fuchs, S. Ohno, J. Sann, M. Rohnke, W. G. Zeier and J. Janek, *Chemistry of Materials*, 2019, **31**, 3745–3755.
- 17 Z. Wang, D. Santhanagopalan, W. Zhang, F. Wang, H. L. Xin, K. He, J. Li, N. Dudney and Y. S. Meng, *Nano Letters*, 2016, **16**, 3760–3767.
- 18 S. K. Otto, L. M. Rieger, T. Fuchs, S. Kayser, P. Schweitzer, S. Burkhardt, A. Henss and J. Janek, *Advanced Materials Interfaces*, 2022, **9**, 2102387.
- 19 C. Ma, Y. Cheng, K. Yin, J. Luo, A. Sharafi, J. Sakamoto, J. Li, K. L. More, N. J. Dudney and M. Chi, *Nano Letters*, 2016, **16**, 7030–7036.
- 20 S. Wenzel, S. J. Sedlmaier, C. Dietrich, W. G. Zeier and J. Janek, *Solid State Ionics*, 2018, **318**, 102–112.
- 21 S. Wenzel, S. Randau, T. Leichtweiss, D. A. Weber, J. Sann, W. G. Zeier and J. Janek, *Chemistry of Materials*, 2016, **28**, 2400–2407.
- 22 A. L. Davis, E. Kazyak, D. W. Liao, K. N. Wood and N. P. Dasgupta, *Journal of The Electrochemical Society*, 2021, **168**, 070557.
- 23 S. Narayanan, U. Ulissi, J. S. Gibson, Y. A. Chart, R. S. Weatherup and M. Pasta, *Nature Communications*, 2022, **13**, 7237.
- 24 A. Paolella, W. Zhu, G. L. Xu, A. La Monaca, S. Savoie, G. Girard, A. Vijh, H. Demers, A. Perea, N. Delaporte, A. Guerfi, X. Liu, Y. Ren, C. J. Sun, J. Lu, K. Amine and K. Zaghib, *Advanced Energy Materials*, 2020, **10**, 2001497.
- 25 L. He, Q. Sun, C. Chen, J. A. S. Oh, J. Sun, M. Li, W. Tu, H. Zhou, K. Zeng and L. Lu, *ACS Applied Materials & Interfaces*, 2019, **11**, 20895–20904.
- 26 J. Tippens, J. C. Miers, A. Afshar, J. A. Lewis, F. J. Q. Cortes, H. Qiao, T. S. Marchese, C. V. Di Leo, C. Saldana and M. T. McDowell, *ACS Energy Letters*, 2019, **4**, 1475–1483.
- 27 Z. Tong, Y.-M. Lai, C.-E. Liu, S.-C. Liao, J.-M. Chen, S.-F. Hu and R.-S. Liu, *ACS Applied Energy Materials*, 2022, **5**, 11694–11704.
- 28 J. A. Lewis, F. J. Q. Cortes, M. G. Boebinger, J. Tippens, T. S. Marchese, N. Kondekar, X. Liu, M. Chi and M. T. McDowell, *ACS Energy Letters*, 2019, **4**, 591–599.
- 29 Q. Yu, D. Han, Q. Lu, Y.-B. He, S. Li, Q. Liu, C. Han, F. Kang and B. Li, *ACS Applied Materials & Interfaces*, 2019, **11**, 9911–9918.
- 30 J. Li, D. Liu, H. Sun, D. Qu, Z. Xie, H. Tang and J. Liu, *Smart-Mat*, 2023, **4**, year.
- 31 N. Fairley, V. Fernandez, M. Richard-Plouet, C. Guillot-Deudon, J. Walton, E. Smith, D. Flahaut, M. Greiner, M. Biesinger, S. Tougaard, D. Morgan and J. Baltrusaitis, *Applied Surface Science Advances*, 2021, **5**, 100112.
- 32 L. He, J. An, S. Oh, K. Watarai, M. Morita, Y. Zhao, Q. Sun, T. Sakamoto, L. Lu and S. Adams, *Cite This: Chem. Mater.*, 2021, **33**, 6841–6852.
- 33 S. P. Ong, Y. Mo, W. D. Richards, L. Miara, H. S. Lee and G. Ceder, *Energy Environ. Sci.*, 2013, **6**, 148–156.
- 34 Y. Zhu, X. He and Y. Mo, *ACS Applied Materials & Interfaces*, 2015, **7**, 23685–23693.
- 35 Q. Zhao, X. Chen, W. Hou, B. Ye, Y. Zhang, X. Xia, J. Wang and C. Yongqi Zhang, *SusMat*, 2022, **2**, 104–112.
- 36 Y. Wu, Y. F. Li, L. Y. Wang, Y. J. Bai, Z. Y. Zhao, L. W. Yin and H. Li, *Electrochimica Acta*, 2017, **235**, 463–470.
- 37 M. Weiss, D. A. Weber, A. Senyshyn, J. Janek and W. G. Zeier, *ACS Applied Materials & Interfaces*, 2018, **10**, 10935–10944.
- 38 C. D. Alt, N. U. C. B. Mü Ller, L. M. Rieger, B. Aktekin, P. Minnmann, K. Peppler and J. Rgen Janek, 2024.
- 39 H. Scher and R. Zallen, *The Journal of Chemical Physics*, 1970, **53**, 3759–3761.
- 40 B. Ozdogru, S. Padwal, B. Bal, S. Harimkar, B. Koohbor and

